

# Shape and Appearance based Spatiotemporal Constraint for LV Segmentation in 4D cardiac SPECT

Ronghua Yang<sup>1</sup>, Majid Mirmehdi<sup>1</sup>, Xianghua Xie<sup>2</sup>, and David Hall<sup>3</sup>

<sup>1</sup> Department of Computer Science, University of Bristol, Bristol BS8 1UB, UK

<sup>2</sup> Department of Computer Science, University of Swansea, Swansea SA2 8PP

<sup>3</sup> Radiology Department, Bristol Royal Infirmary, Bristol BS2 8HW, UK

**Abstract.** We propose a novel shape and appearance based spatiotemporal constraint and combine it with a level set based deformable model, which can be used for Left Ventricle segmentation in 4D gated cardiac SPECT, particularly in the presence of perfusion defects. The model incorporates appearance in addition to shape information into a *soft-to-hard* probabilistic constraint, and utilizes spatiotemporal regularization via a Maximum A Posteriori framework. This constraint force allows more flexibility than the rigid forces of shape constraint-only schemes, as well as other state-of-the-art joint shape and appearance constraints. We present comparative results to illustrate the improvement gain.

**Key words:** spatiotemporal 4D segmentation, constrained deformable model, gated cardiac SPECT

## 1 Introduction

The segmentation of LV borders allows quantitative analysis of perfusion defects and cardiac function, and is thus of significant importance to diagnosis and clinical study. In SPECT, perfusion defects have low or no contrast against the background, thus the accurate determination of the LV borders around the defect is difficult and prior knowledge of LV shape is usually required to estimate such defective borders. Additionally, the image data often contains hot structures in the proximity of the LV, considered as perfusion artifacts that impose similar difficulties for correct LV segmentation. Further, due to partial volume effect, the images at end-systole tend to look brighter than end-diastole, known as the artifact of myocardial brightening, which means prior knowledge of cardiac motion is required to estimate LV borders. In this paper, we address these problems and propose an automated and reliable segmentation approach that detects LV borders in the face of perfusion defects and artifacts, as well as cardiac motion, in 4D cardiac SPECT.

As spatiotemporal methods offer the advantages of time consistent segmentation [1], a variety of such methods have been proposed for LV segmentation on gated cardiac SPECT. Debreuve et al. [1] and Charnoz et al. [2] took into account all the timeframes of the sequence to cope with background noise. Montagnat et al. [3] used a pre-determined 4D shape model registered onto the input image sequence under shape and temporal constraints. Kohlberger et al. [4] applied a level set model to search LV borders under a statistical constraint, similar to that introduced in [5]. The model in [6] is extended

from [4] and inferred the constraint by utilizing a kernel density estimator as suggested in [7] instead of the multivariate Gaussian model.

The main limitations of the above models would surface if they deal with pathological cases. For example, [1, 2] assumed that the LV has constant pixel values, [3] relied on its own rigidity to hypothesize on the defective borders, and the constraints in [4, 6] were applied to the models rigidly, i.e. with equal strength everywhere. Such shortcomings can compromise the accuracy of the estimate, especially on LVs with local variations and medium to severe perfusion defects. Further, the constraints of these models are shape based, with no mechanism proposed to incorporate appearance information correlating to the shape in the constraint forces. Since the shape of a perfusion does not always correspond to the LV shape in the presence of defects, we argue that these shape based constraints still lack flexibility to deal with abnormal perfusion and hence can compromise segmentation accuracy. Appearance information, in addition to shape, should be considered.

In [8], Rousson and Paragios proposed a constraint via finding maximum probability density function (pdf) of the shape and combined it with a level set model for object detection in optical images with noisy or missing data. This Self-Constrained Geodesic Active Regions model is hereafter referred to as SCGAR. Their probabilistic approach takes into account shape variability, producing a soft-to-hard force, which allows a wider range of shape variations than the models in [4, 6]. We will use this methodology as part of our approach towards LV detection in cardiac SPECT as LV shapes contain large degrees of irregular inter-class variations [9].

For more reliable application in SPECT, we borrow from the soft-to-hard probabilistic framework of SCGAR and replace its shape based pdf objective function with a posterior that considers the shape and appearance of the whole sequence, leading to a novel shape and appearance based spatiotemporal constraint derived with MAP estimation. Instead of globally aligning shapes when evaluating the pdf in SCGAR, we apply a global-to-local alignment. Meanwhile, as in [4, 6], Principal Component Analysis (PCA) is employed in our model to reduce data dimension and statistically depict shape variations. However unlike [4, 6], instead of applying PCA to the whole level set domain, we apply it to the deformation fields of the level sets, characterized by transformation parameters, to further reduce the data space and allow better control over temporal shape variations. Compared with current works on joint shape and appearance constraints such as [10–14], our soft-to-hard constraint allows more flexibility than their rigid forces. Additionally, we argue that the probabilistic framework makes better use of the correlation between shape and appearance than those that linearly combine the two, e.g. [10–13].

In all, we present a model combining a recently proposed general-purpose deformable model for boundary detection, namely Charged Active Contour based on Electrostatics (CACE) [15], with a constraint that is capable of incorporating prior knowledge in correlated shape and appearance, as well as spatiotemporal variations. This is designed to cope with the irregularities in variations of LV shapes and motions and the extremely fuzzy gradients due to (temporal) perfusion defects and artifacts in cardiac SPECT. We refer to this combined model as Constrained CACE (CCACE).

CACE is a general-purpose active contour model introduced by Yang et al in [15] that incorporates particle based electrostatic interactions into the geometric active contour framework. It can be used for object boundary detection in a variety of images. Embedded in level sets, CACE propagates under the influence of a bi-directional force field that simulates the electrostatic interaction between an image-derived point charge field and a charged contour. The force field leads the contour towards object boundaries and dynamically adapts as the contour evolves. It brings flexibility in initialization and better curve propagation towards object boundaries. The level set  $\phi$  evolution of CACE is

$$\frac{\partial \phi}{\partial t} = w_c g \kappa |\nabla \phi| - (1 - w_c) \mathbf{J} \cdot \nabla \phi \quad (1)$$

where  $w_c$  is a real positive constant,  $g$  is an edge stopping function of the input image,  $\kappa$  denotes the curvature of the contour, and  $\mathbf{J}$  is the dynamic electrostatic force. For more details of CACE the reader is referred to [15]. As mentioned earlier, we build CCACE on the CACE framework and effectively CCACE is CACE with the addition of specific constraints for 4D LV segmentation.

## 2 Proposed CCACE Model

**An Overview** - The proposed model comprises two stages: training and segmentation. Through the training stage, a set of pixel-wise Gaussian priors and spatiotemporal priors are obtained. The Gaussian priors include a prior image, a prior shape, an image variation term, a shape variation term, and the correlation between image and shape. The spatiotemporal priors are the products of applying PCA to global-to-local transformation parameters of the shape variations, and include mean of the parameters, modes of variations (or eigenmodes), weights for the eigenmodes, as well as the covariance of the weights.

During segmentation, an initial surface embedded in level sets is placed in the input image. A constraint force is derived by finding the maximum of the multivariate pdf of the input image and the level sets based on the Gaussian priors from the training stage. As the level sets evolve, the pdf continuously updates by aligning the joint priors (prior image and shape) with the input image and the level sets via global-to-local transformations to enable meaningful evaluation of the pdf. The alignment is regularized by the prior distribution over a set of *spatiotemporal parameters* of the transformations. The force derived from this regularized multivariate pdf, effectively a posterior, is a shape and appearance based spatiotemporal constraint obtained via MAP estimation. The evolving level sets update according to the combination of CACE forces and this constraint to reach (and hypothesize missing or defective) LV borders. Next, we discuss the training and segmentation stages in detail, followed by experimental results in gated cardiac SPECT.

### 2.1 Training

A training set  $\mathcal{M} = \{(\tilde{\mathbf{I}}_i, \tilde{\phi}_i) : i \in [1, N]\}$  of  $N$  gated SPECT samples is constructed from manually labelled 4D sequences. Each sample  $(\tilde{\mathbf{I}}_i, \tilde{\phi}_i)$  consists of a pair - an image

sequence  $\dot{\mathbf{I}}_i$  and its corresponding LV shape sequence  $\dot{\phi}_i$ , where  $\dot{\mathbf{I}}_i$  is the  $i^{\text{th}}$  training image sequence, and  $\dot{\phi}_i$  is the  $i^{\text{th}}$  training shape sequence embedded in level sets constructed by manually labelling on  $\dot{\mathbf{I}}_i$ . Each training sequence consists of  $K$  timeframes, i.e.  $\dot{\mathbf{I}}_i = \{\dot{I}_{i,k} : k \in [1, K]\}$  and  $\dot{\phi}_i = \{\dot{\phi}_{i,k} : k \in [1, K]\}$ . Any known defect-free sequence can be selected as the reference shape sequence  $\dot{\phi} = \{\dot{\phi}_k : k \in [1, K]\}$ . Each training shape  $\dot{\phi}_{i,k}$  is globally and locally aligned towards the corresponding timeframe of the reference shape sequence, i.e.  $\dot{\phi}_k$ , via the global-to-local registration technique proposed in [16]<sup>4</sup>, in order to reduce nonlinearity to fit in a Gaussian prior. The transformations recovered from these shape registrations are then applied to the training images accordingly to sustain the correspondence between training images and shapes. From the aligned training set we derive two sets of priors: pixel-wise Gaussian priors and spatiotemporal priors.

**Gaussian Priors** - We compute pixel-wise means of images  $\bar{\mathbf{I}} = \{\bar{I}_k : k \in [1, K]\}$ , image standard deviations  $\bar{\sigma}_I = \{\bar{\sigma}_{I_k} : k \in [1, K]\}$ , means of the shapes  $\bar{\phi} = \{\bar{\phi}_k : k \in [1, K]\}$ , shape standard deviations  $\bar{\sigma}_\phi = \{\bar{\sigma}_{\phi_k} : k \in [1, K]\}$ , and the correlation coefficients between image and shape  $\bar{\rho} = \{\bar{\rho}_k : k \in [1, K]\}$ .  $\bar{\mathbf{I}}$  and  $\bar{\phi}$  are also referred to as the prior image/appearance and prior shape sequence respectively. As the training shapes are locally aligned, there is risk of bias in the priors towards the reference  $\dot{\phi}$ , the impact of which on the model performance is however insignificant, as will be mentioned later at segmentation stage. The prior image and shape sequences of our training set, for  $K = 8$  and  $N = 15$ , are shown in Fig. 1.

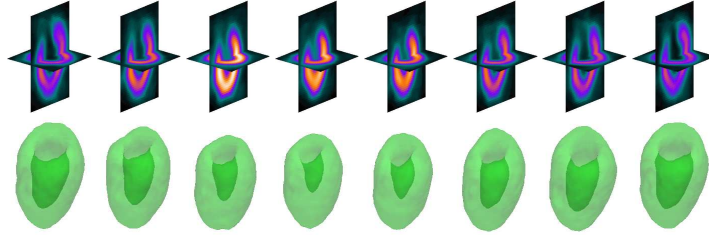


Fig. 1. From left: timeframes 1-8. From top: prior image and shape sequence.

**Spatiotemporal Priors** - We seek parameterized temporal correlation among the spatial variations by applying two levels of PCA to a set of transformation parameters that describe how the training shapes  $\dot{\phi}_i$  vary from the prior shape  $\bar{\phi}$ . These transformation parameters, denoted as  $\{\Theta_{i,k} : (i, k) \in [1, N] \times [1, K]\}$ , are recovered from mapping the prior shape  $\bar{\phi}$  into training shapes  $\dot{\phi}_i$ , again via the global-to-local registration technique proposed in [16]. The distribution of  $\Theta_{i,k}$  can be used to regularize the segmentation later during which the joint priors  $(\bar{\mathbf{I}}, \bar{\phi})$  are aligned towards the input image and level sets.

PCA is then applied to the recovered transformation parameters  $\{\Theta_{i,k} : i \in [1, N]\}$  at each timeframe  $k$  individually, each giving a mean  $\bar{\Theta}_k$ , eigenmodes  $\mathbf{P}_k$ , and weights

<sup>4</sup> We use a rigid transformation and a  $16 \times 16 \times 12$  IFFD grid with single resolution scheme.

for the eigenmodes  $\{\hat{\mathbf{b}}_i : i \in [1, N]\}$ . A further PCA is then applied to these weights of all timeframes, i.e.  $\{\hat{\mathbf{b}}_{i,k} : (i, k) \in [1, N] \times [1, K]\}$ , and produces second-level eigenmodes  $\mathbf{Q}$  and weights  $\{\hat{\mathbf{v}}_i : i \in [1, N]\}$ . The weights from the first PCA statistically depict shape variations of every timeframe, and the second PCA on them produces parameters that control their spatiotemporal variations. This is similar to Cootes et al. [17] where an appearance model is built by applying second-level PCA to the results of a first-level PCA on shape and gray-level intensity data respectively. These two levels of PCA give an approximation for a new set of transformation parameters  $\Theta_k$ , i.e.  $\Theta_k = \bar{\Theta}_k + \mathbf{P}_k \mathbf{Q}_k \mathbf{c}$ , where  $\mathbf{Q} = [\mathbf{Q}'_1 \dots \mathbf{Q}'_K]'$  and  $\mathbf{c}$  is a varying parameter to be determined. As it indirectly controls both spatial and temporal variations of the sequence through affecting its transformations, we refer to  $\mathbf{c}$  as the *spatiotemporal parameters*. Assuming normal distribution, the prior distribution of  $\mathbf{c}$  is

$$P_c(\mathbf{c}) = \left( \sqrt{(2\pi)^n |\mathbf{U}|} \right)^{-1} \exp\left(-\frac{1}{2} \mathbf{c}' \mathbf{U}^{-1} \mathbf{c}\right) \quad (2)$$

where  $n$  is the number of modes of  $\mathbf{Q}$  and  $\mathbf{U}$  is the covariance matrix whose diagonal comprises the eigenvalues obtained from the second-level PCA.

## 2.2 Constrained Segmentation

We now outline the derivation of our proposed constraint force based on the priors obtained during training and then give the combined formulation of CCACE.

**Shape and Appearance based Spatiotemporal Constraint** - We use a variational framework to derive the constraint force that helps evolve the level sets to optimize a posterior, defined as the product of a shape and appearance multivariate pdf and the prior distribution over the spatiotemporal parameters. The posterior measures the probability of the input image and shape to occur in a normal distribution characterized by the Gaussian priors obtained in training, under spatiotemporal regularization through the prior distribution.

Given the input image sequence  $\mathbf{I} = \{I_k : k \in [1, K]\}$  and the evolving level sets  $\phi = \{\phi_k : k \in [1, K]\}$  placed on the image, the posterior is defined as:

$$P_A(\phi, \mathbf{c}) = \prod_{k=1}^K \left( (2\pi) \sqrt{|\Sigma_k|} \right)^{-1} \exp\left(-\frac{1}{2} \mathbf{a}_k^T \Sigma_k^{-1} \mathbf{a}_k\right) P_c(\mathbf{c}), \quad (3)$$

$$\text{where } \mathbf{a}_k = \begin{bmatrix} a_{\phi_k} \\ a_{I_k} \end{bmatrix} = \begin{bmatrix} (1 - \lambda_I) & 0 \\ 0 & \lambda_I \end{bmatrix} \left( \begin{bmatrix} s_k \phi_k \\ I_k \end{bmatrix} - \begin{bmatrix} \bar{\phi}_k(T) \\ \bar{I}_k(T) \end{bmatrix} \right),$$

$$\Sigma_k = \frac{1}{1 - \bar{\rho}_k^2(T)} \begin{bmatrix} \bar{\sigma}_{\phi_k}^2(T) & \bar{\rho}_k(T) \bar{\sigma}_{\phi_k}(T) \bar{\sigma}_{I_k}(T) \\ \bar{\rho}_k(T) \bar{\sigma}_{\phi_k}(T) \bar{\sigma}_{I_k}(T) & \bar{\sigma}_{I_k}^2(T) \end{bmatrix}.$$

$T$  is the simplified representation of  $T(\Theta_k; \mathbf{x})$ , which denotes the transformation model of the registration in [16], where  $\mathbf{x}$  are the pixel locations. The joint priors  $(\bar{\mathbf{I}}, \bar{\phi})$  are aligned with the input appearance and shape  $(\mathbf{I}, \phi)$  through  $T(\Theta_k; \mathbf{x})$ , for  $k \in [1, K]$ . The transformations act on the priors so that the derived constraint force applies straightforwardly to the level sets and can be directly combined with CACE. Note that

the impact of potential bias in the priors towards the reference  $\phi$  is largely alleviated via the alignment here. Positive constant  $\lambda_I$  balances the contributions from image and shape.  $\Sigma_k$  is the covariance between image and shape, and  $s_k$ , a component of  $\Theta_k$ , is the scaling factor. The reason for applying  $s_k$  to  $\phi_k$  is that level set representation is not invariant to scaling - see [8] for details. As both  $\phi$  and  $\mathbf{c}$  are unknown, a coupled optimisation task is possible, with  $E_A(\phi, \mathbf{c})$  as the objective function:

$$\langle \tilde{\phi}, \tilde{\mathbf{c}} \rangle = \arg \min_{\phi, \mathbf{c}} E_A(\phi, \mathbf{c}) = \arg \min_{\phi, \mathbf{c}} \left( - \int_{\mathbf{X}} \log(P_A(\phi, \mathbf{c})) dx \right) \quad (4)$$

$\mathbf{X}$  represents all the possible locations in the shape domain<sup>5</sup>. The posterior based objective function in (4) considers both shape and appearance information and is evaluated with variations between the joint priors and the input shape and appearance taken into account. In particular, only spatiotemporally plausible variations are accounted for owing to the regularization that biases the transformation parameters towards their most probable values. This keeps the model within plausible shapes and motions. The level sets evolve towards the maximum of the posterior to give the best probabilistic estimate over the shape in the input image.

**Level Set Evolution of CCACE** - Combining the constraint component with CACE, the motion equations for CCACE are given in (5) and (6), through which  $\phi$  and  $\mathbf{c}$  update iteratively and simultaneously until equilibrium:

$$\frac{\partial \phi_k}{\partial t} = \lambda_c \underbrace{\left( w_c g \kappa |\nabla \phi_k| - (1 - w_c) \mathbf{J} \cdot \nabla \phi_k \right)}_{CACE} \quad (5)$$

$$+ (1 - \lambda_c) \frac{s_k}{1 - \bar{\rho}_k^2(T)} \left( \underbrace{(1 - \lambda_I) \frac{s_k \phi_k - \bar{\phi}_k(T)}{\bar{\sigma}_{\phi_k}^2(T)}}_{\text{Shape}} - \underbrace{\lambda_I \bar{\rho}_k(T) \frac{I_k - \bar{I}_k(T)}{\bar{\sigma}_{\phi_k}(T) \bar{\sigma}_{I_k}(T)}}_{\text{Appearance}} \right)$$

$$\frac{\partial \mathbf{c}}{\partial t} = - \left( \frac{\partial E_A(\phi, \mathbf{c})}{\partial \Theta} \right)' [\mathbf{Q}'_1 \mathbf{P}'_1 \dots \mathbf{Q}'_K \mathbf{P}'_K] - \mathbf{U}^{-1} \mathbf{c} \quad (6)$$

where  $\Theta = \{\Theta_k : k \in [1, K]\}$ . In (5), the first term represents the data-driven evolution of CACE, while the second is the constraint force, derived based on (4), with  $\lambda_c$  balancing the contributions from the two. The constraint force consists of a shape and an appearance term.  $\mathbf{c}$  also updates according to (6) at each iteration of  $\phi$ 's evolution to keep the joint priors aligned with the input appearance and shape.

According to (5), the level sets evolve under the confluence of the force field in CACE and the proposed constraint force. The shape term drives the level sets towards the aligned prior shapes. In the denominator, the squared deviation allows shape variability, hence the shape driving force is applied in a soft-to-hard pattern. Meanwhile, the appearance term penalizes or strengthens the constraint force depending on the correlation between image and shape. The more distant the input image from the aligned prior image, the stronger the term is, where image variability is also taken into account. It plays the role of an extra criterion for constraining the level sets and brings further flexibility in the constraint.

<sup>5</sup> Note that the level set shape domain coincides with the image domain.

Since the closer the initial shape to the final shape to be recovered, the more efficient the segmentation process is, we seek a shape estimate over the input image for the level set evolution to start with. This is done by aligning the prior image towards the input image, via minimizing  $E_A(\phi, \mathbf{c})$  with  $\lambda_I = 1$  ( $\phi$  is ignored). The recovered spatiotemporal parameters are taken as the initial values for  $\mathbf{c}$ 's evolution. The recovered transformations are then applied to the prior shape, giving the shape estimate.

### 3 Experimental Results

We used 15 sets of gated cardiac SPECT sequences of healthy LVs with normal perfusion for training, and applied CCACE to another 14 sequences for performance evaluation, two of which are pathological cases and present perfusion defects. All patient studies were clinical studies acquired following standard protocols. The resolution of the data is  $64 \times 64 \times \alpha \times 8$  where  $\alpha$  varies between 25 and 58. Throughout the experiments, we set  $\lambda_c = 0.4$  and  $\lambda_I = 0.5$  which are determined empirically. For each  $\mathbf{P}_k$  and  $\mathbf{Q}$ , the 10 most significant modes were chosen to explain 95% of variations. For comparison, we also implemented SCGAR based on [8].

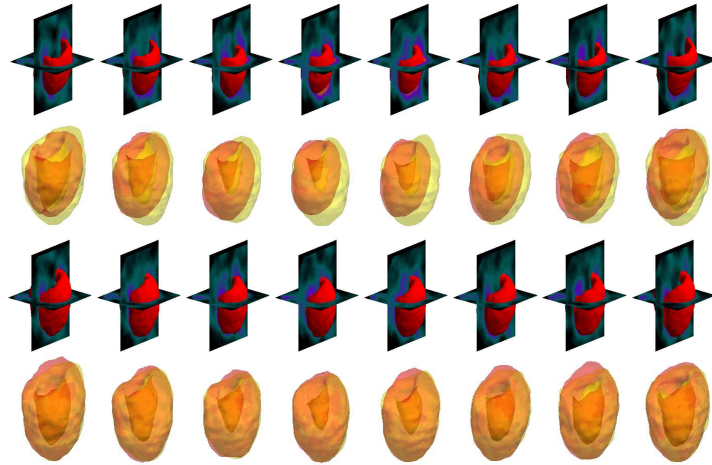


**Fig. 2.** SCGAR (top 2 rows) and CCACE (bottom 2 rows) on gated cardiac SPECT with severe perfusion defects. Model results are in red and ground truth in yellow.

Fig. 2 shows an example of the results for SCGAR and CCACE for an LV with severe myocardial infarction in the inferior wall (consistent perfusion defects present throughout the sequence as well as perfusion artifacts due to liver uptake). Fig. 3 shows the results in 2D slices where the SCGAR model can be seen to merge over defect areas as marked by white arrows, while CCACE sustains a plausible shape and successfully differentiates the epicardial from the endocardial borders in these areas. SCGAR has large deviation from the borders in the lateral segments as marked by green arrows,

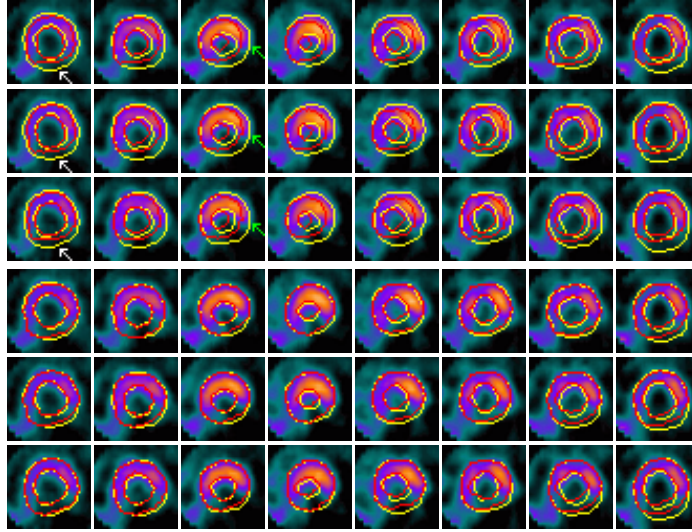


**Fig. 3.** SCGAR results (top three rows) and CCACE (bottom three rows) on slices selected from the sequence. From left: timeframes 1-8. From top (each group): three slices at different locations of the LV. Model results in red and ground truth in yellow.

while CCACE converges more closely around them. This shows CCACE has more flexibility as its constraint is more alert to defect regions while less sensitive to lateral segments.

Fig. 4 shows the model results on an example of an LV with a long apical region in particular. SCGAR fails to produce an accurate estimate over the LV especially in the apical regions as marked by black arrows, whereas CCACE has achieved better results.

**Quantitative comparison and Timing** - The Jaccard's coefficients of the results for SCGAR on the two examples above are 62.3% and 48.9%, and that for CCACE are 85.8% and 90.6%. Across the 14 SPECT sequences, the average accuracy of CCACE is 88.0%, with  $\sigma = 4.9\%$ , and that of SCGAR is 59.8% with  $\sigma = 9.5\%$ . All the datasets were manually labelled by an expert or the author and subsequently adjusted and approved by the expert as the ground truth.

Using a 2.8 GHz Linux PC running uncompiled Matlab code, the training stage of CCACE takes 3hr and 43mins. The average computation time for segmentation is 249s, while that for SCGAR is 136s.

## 4 Conclusions

CCACE probabilistically determines LV boundaries based on image gradients under a shape and appearance based spatiotemporal constraint. CCACE a) makes use of global-to-local rather than global transformation to account for larger range of variability, b) applies appearance in addition to shape information, and c) has MAP spatiotemporal

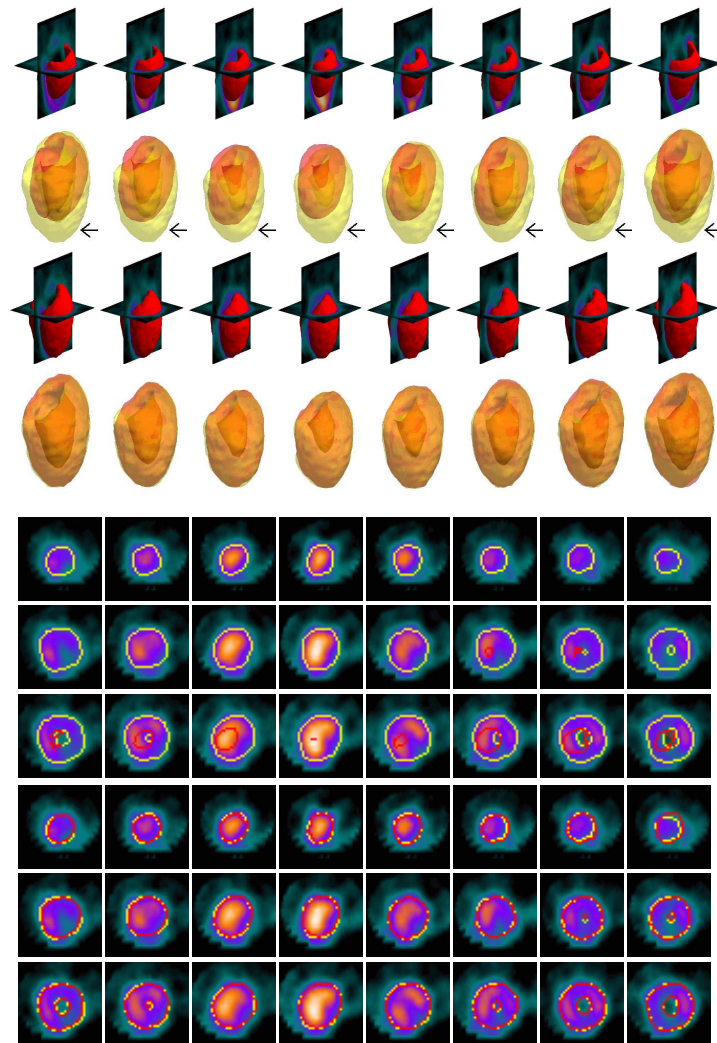


**Fig. 4.** SCGAR (rows 1-2 and 5-7) and CCACE (rows 3-4 and 8-9) on an LV with a long apical region.

regularisation, i.e. takes the temporal domain into consideration. The first two aspects allow more flexibility in the constraint while the third brings more robustness to irregularities in temporal variations of the data.

## References

1. Debreuve, E., Barlaud, M., Aubert, G., Laurette, I., Darcourt, J.: Space-time segmentation using level set active contours applied to myocardial gated spect. *MI* **20** (2001) 643–659
2. Charnoz, A., Lingrand, D., Montagnat, J.: A levelset based method for segmenting the heart in 3D+T gated SPECT images. *FIMH* **2674** (2003) 87–100
3. Montagnat, J., Delingette, H.: 4D deformable models with temporal constraints: Application to 4D cardiac image segmentation. *MIA* **9** (2005) 87–100
4. Kohlberger, T., Cremers, D., Rousson, M., Ramaraj, R., Funka-Lea, G.: 4D shape priors for a level set segmentation of the left myocardium in SPECT sequences. In: *MICCAI*. Volume 9. (2006) 92–100
5. Leventon, M., Grimson, W., Faugeras, O.: Statistical shape influence in geodesic active contours. In: *CVPR*. (2000) 316–323
6. Timo, K., Gareth, F., Vladimir, D.: Soft level set coupling for LV segmentation in gated perfusion SPECT. In: *MICCAI*. Volume 10. (2007) 327–334
7. Rousson, M., Cremers, D.: Efficient kernel density estimation of shape and intensity priors for level set segmentation. In: *MICCAI*. Volume 8. (2005) 335–342
8. Rousson, M., Paragios, N.: Shape priors for level set representations. In: *ECCV*. (2002) 78–92
9. Fisher, V., Lee, R., Gourin, A., Bolooki, H., Stuckey, J., Kavalier, F.: Muscle fiber length: A determinant of left ventricular contraction pattern. *Am J Physiol* **211** (1966) 301–306
10. Huang, X., Li, Z., Metaxas, D.: Learning coupled prior shape and appearance models for segmentation. In: *MICCAI*. (2004) 60–69
11. Ben-Ari, R., Aiger, D.: Geodesic active contours with combined shape and appearance priors. In: *ACIVS*. (2008) 494–505
12. Gleason, S., Abidi, M., Sari-Sarraf, H.: Probabilistic shape and appearance model for scene segmentation. In: *ICRA*. Volume 3. (2002) 2982–2987
13. Litvin, A., Karl, W., Shah, J.: Shape and appearance modeling with feature distributions for image segmentation. In: *ISBI*. (2006) 1128–1131
14. Yang, J., Duncan, J.: 3D image segmentation of deformable objects with shape-appearance joint prior models. In: *MICCAI*. (2003) 573–580
15. Yang, R., Mirmehdi, M., Xie, X.: A charged active contour based on electrostatics. In: *ACIVS*. (2006) 173–184
16. Huang, X., Paragios, N., Metaxas, D.: Shape registration in implicit spaces using information theory and free form deformations. *PAMI* **28** (2006) 1303–1318
17. Cootes, T., Edwards, G., Taylor, C.: Active appearance models. In: *ECCV*. Volume 2. (1998) 484–498